THE ASTROPHYSICAL JOURNAL, 524:469–482, 1999 October 10

PHOTOSPHERIC AND CHROMOSPHERIC GAS MOTIONS AROUND A DARK FILAMENT

TETSUYA MAGARA[1] AND REIZABURO KITAI
Hida Observatory, Faculty of Science, Kyoto University, Kamitakara, Gifu 506-1314, Japan
Received 1999 January 4; accepted 1999 May 20

ABSTRACT

In this paper, we investigate how photospheric material moves below a dark filament, and we study chromospheric gas motions inside the filament. In the photosphere we trace granular motions by means of a local correlation tracking (LCT) technique to derive horizontal velocity field, while inside the filament we obtain the line-of-sight velocity field by subtracting a blueshifted Hα image from a redshifted Hα image. We find that a typical value of horizontal photospheric velocity is 1 km s^{-1}, and its divergence map maintains a large-scale pattern during several hours. We also find that photospheric motions around a filament channel are random in space and changeable in time. As for the motion inside the filament, our results show that there is an area of upward motions at one side of the filament axis and an area of downward motions at the other side, which means that filament material has a helical motion inside the filament. We think that these results provide new important information on theories of filament formation.

Subject headings: Sun: atmosphere — Sun: filaments — Sun: granulation — Sun: magnetic fields

1. INTRODUCTION

Filaments are probably one of the most conspicuous things observed in the solar atmosphere. When they are observed in some particular line such as Hα, filaments have a dark, long, extended body on the solar disk, whereas they are observed to have a bright archlike structure at the solar limb. In the latter case, they are called prominences. Macroscopically, filaments are usually in a quiet state, although they sometimes suddenly enter a dynamical stage, erupting upward and finally disappearing (filament eruption). For solar physicists, it is an interesting and important problem to understand the nature of such filaments, so many studies have been done on this topic.

Although filament eruptions are those events that occur in the upper layer of the solar atmosphere, the corona, it has been understood that the effect of the lower layer, the photosphere, on such eruptions is very important. Since the mass density of the photosphere is much higher than that of the corona, even slow motions in the photosphere can produce flow speeds in the corona that are fast enough to violate quasi-static evolution (Priest & Forbes 1990). In this respect, there must be a medium by which photospheric perturbations are transferred into the corona. This medium also makes a significant contribution to the formation of filaments. On the basis of detailed observations, it is now widely believed that the medium is a magnetic field, and hence a considerable number of studies have been done on the modeling of filaments in terms of magnetic field.

Since the interaction between photospheric motions and magnetic fields extending into the corona plays an important role in the dynamics of filaments, it is natural to investigate how photospheric material moves below a filament and how coronal magnetic fields evolve when a particular kind of photospheric motion is imposed at their footpoints. Observationally photospheric material has been reported to converge toward a magnetic neutral line located just below a filament axis (filament channel) (Martin, Livi, & Wang 1985). This leads to a theoretical model in which such converging photospheric motions produce the configuration of magnetic fields that can support a dense plasma in the corona (van Ballegooijen & Martens 1989; Anzer 1990; Inhester, Birn, & Hesse 1992; Choe & Lee 1992; Ridgway & Priest 1993; Priest, Parnell, & Martin 1994; Priest, van Ballegooijen, & MacKay 1996; Kuijpers 1997). In this model, two regions of opposite magnetic polarities approach each other (caused by converging flows), and then magnetic reconnection occurs between them, forming a dip of magnetic fields above a magnetic neutral line to support a dense plasma against gravitational force. This mutual approach of opposite-polarity regions also causes flux cancellations in the photosphere. In addition, some of the work on this model shows filament eruptions may be brought about by such converging motions (van Ballegooijen & Martens 1989; Choe & Lee 1992; Ridgway & Priest 1993).

Prompted by this kind of work, in order to provide other important information on photospheric motions around a filament channel, this paper examines the photospheric velocity field below a dark filament directly, by tracing the motion of granules. The essence of this technique is to calculate a correlation between two fine granulation images observed at different times and then find the displacement between these images. This technique is called local correlation tracking (LCT) and has already been used in many works to investigate photospheric motions. For example, November (1986) made a detailed description of this technique, November & Simon (1988) considered the procedure for reducing atmospheric seeing effects, Simon et al. (1988) studied the relation between photospheric flows and the magnetic field distribution in the solar surface by using SOUP data, Brandt et al. (1988) found vortex photospheric motions, and Title et al. (1989) discussed the differences between photospheric motions in magnetic regions and those in field-free regions. Recently, Kitai et al. (1997) investigated photospheric motions around a simple sunspot, and Ueno & Kitai (1997) studied the nature of mesogranules using a time sequence of photospheric velocity maps.

The organization of this paper is as follows. In the next section we show the data used in this study. The data analysis is described in § 3, and our results are shown in § 4.

[1] magara@kusastro.kyoto-u.ac.jp

Finally, we discuss the connection between our results and theories of filament formation in § 5.

2. DATA

The observations were made on 1998 May 21/22 with the Domeless Solar Telescope (DST) at Hida Observatory in Japan. We observed an area around a dark filament, the position of which is shown in Figure 1 (white arrow). This filament was on the whole in a quiet state during the observation, although there were continual small-scale motions in it. Throughout one sequence of observation, we took G-band granulation images with and without a dark line, Hα filament images with a dark line, and three types of chromospheric images (see below).

2.1. *Granulation Images*

We took granulation images in the G band ($\lambda = 4308$ Å) with a video CCD camera, TM 9700NMH, made by Takenaka System Co. Ltd. Japan (we call this a G-band camera) to investigate photospheric motions. These images have 512×512 pixels in 8 bits. They were selected by a Real-Time Frame Selector (RTFS) attached on the DST. RTFS is a device used to evaluate the quality of images at a rate of about 15 frames s^{-1} and select the best images in real time without any time delay (for details see Kitai et al. 1997). The average time interval between consecutive images in the time sequence is therefore about 15 s. As for the resolution of images, 1 pixel corresponds to 0.″33 or about 240 km on the solar disk. There are two types of G-band images, one with a dark line on the image and the other without it. This dark line was produced by a fiducial mark placed in an intermediate focal plane (i.e., the slit of the spectrograph). The former type of image was used for the co-alignment of a G-band granulation image and an Hα filament image (see §§ 2.2 and 3.2), and the latter was used for calculating the correlation between G-band images. Examples of these two types of images are shown in Figure 2.

2.2. *Dark Filament Images*

In order to determine the relative position of a dark filament on a granulation image, we also observed filament images with a dark line on them in Hα($\lambda = 6562.8$ Å), using a Lyot filter. These Hα filament images had been taken with another CCD camera of type similar to the G-band camera (we call this an Hα camera) slightly before the G-band granulation images were taken. The pixel size in Hα filament images is 0.″69, or about 500 km on the solar disk. An example of these images is shown in Figure 3, where a dark line can be seen.

2.3. *Three Types of Chromospheric Images*

In order to investigate line-of-sight motions inside the filament, we observed three types of chromospheric images with the Lyot filter mentioned in § 2.2 (slightly after the Hα filament images shown in § 2.2 were observed): Hα center images ($\lambda = 6562.8$ Å), redshifted images ($\lambda = 6562.8 + 0.6$ Å), and blueshifted images ($\lambda = 6562.8 - 0.6$ Å). All these

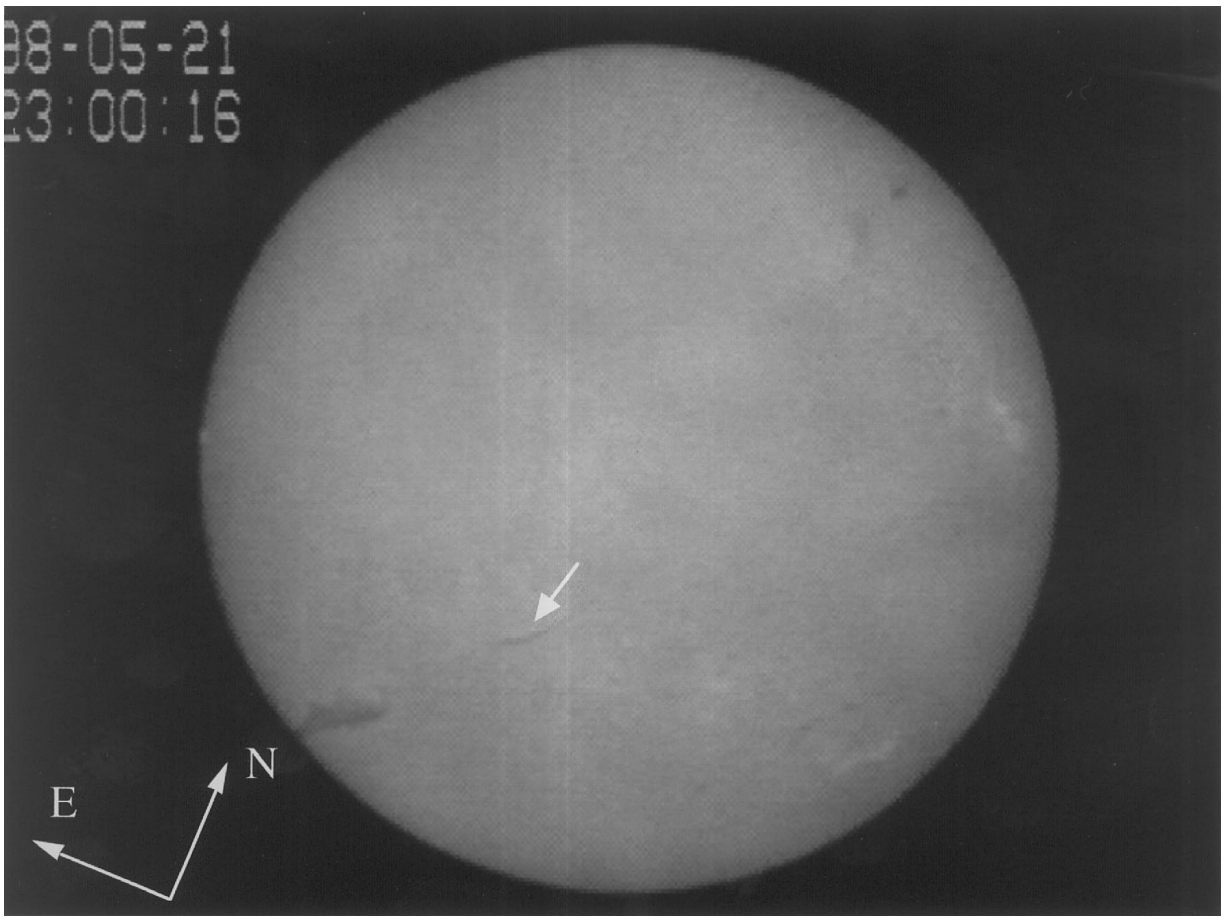

FIG. 1.—Dark filament observed on 1998 May 21 UT with the DST at Hida Observatory in Japan. A white arrow shows the position of the filament on the solar disk. North is up and east is to the left.

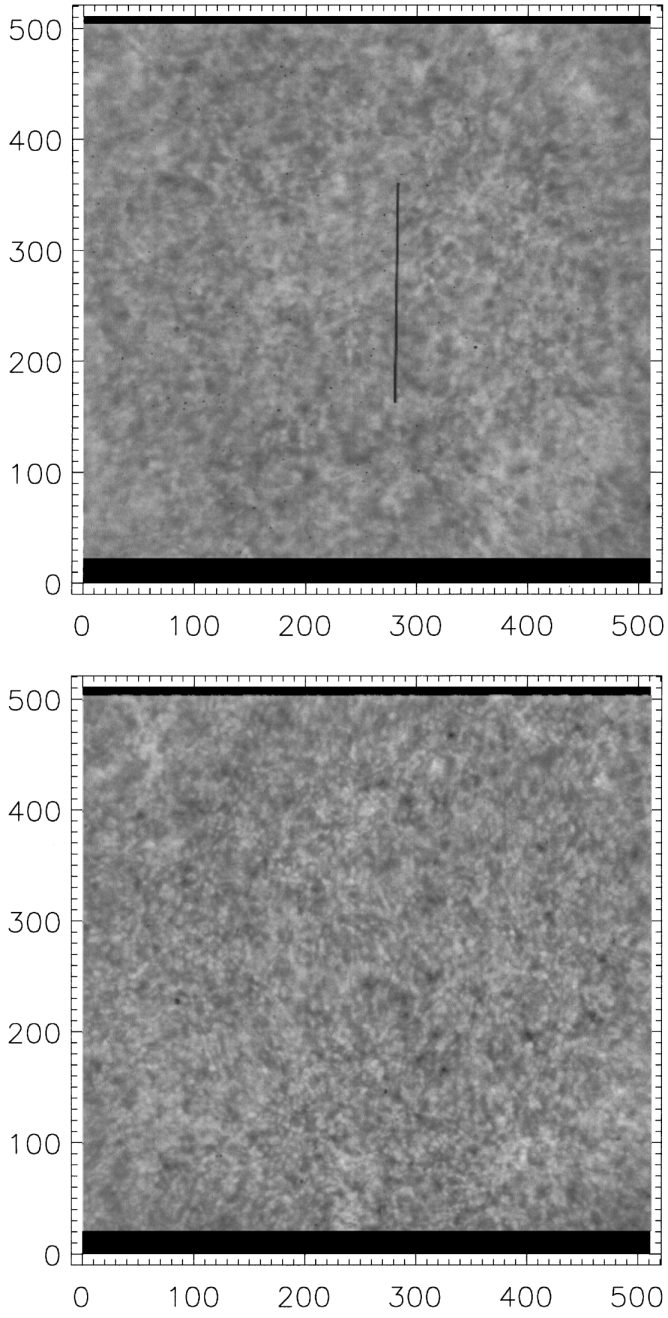

FIG. 2.—Examples of granulation images in the G band ($\lambda = 4308$ Å). Pixel dimensions are 512 × 512, and 1 pixel corresponds to 0.″33 or about 240 km on the solar disk. The upper panel shows the case with a dark line on the image, and the lower panel is without it.

images were taken with the Hα camera and rearranged to have 640 × 480 pixels. For each type, the time interval between consecutive images in the time sequence is about 20 s. The pixel size of images is 0.″69, or about 500 km on the solar disk. Examples of these three types of chromospheric images are shown in Figure 4.

3. DATA ANALYSIS

3.1. *Photospheric Velocity Field*

For the derivation of photospheric velocity field, we followed the analysis procedure described in Kitai et al. (1997). A detailed account of this procedure is given below.

The first step is to divide a granulation image into many subsections. The granulation image has 512 × 512 pixels (see § 2.1); we divided part of this image into 27 × 24 side-by-side subsections, each of which has 15 × 15 pixels (see Fig. 5). From now on, each subsection is represented by a pair of integers (x_0, z_0), where x_0 is the column number counted from the left side and z_0 is the row number counted from the bottom.

The cross-correlation between two granulation images observed at different times (t and $t + \delta t$) is calculated for each subsection. According to Yi & Molowny-Horas (1992), the linear cross-correlation would be the most suitable one for solar granulation. For a subsection (x_0, z_0), this is expressed as

$$\mathrm{CC}(\delta x, \delta z, x_0, z_0) = \frac{\iint_{S_0} I_t(x, z) I_{t+\delta t}(x + \delta x, z + \delta z)\,dx\,dz}{\sqrt{\iint_{S_0} I_t^2(x, z)\,dx\,dz}\sqrt{\iint_{S_0} I_{t+\delta t}^2(x + \delta x, z + \delta z)\,dx\,dz}}, \quad (1)$$

where CC is the coefficient of cross-correlation, I_t and $I_{t+\delta t}$ are the intensities at t and $t + \delta t$, $(\delta x, \delta z)$ is the relative displacement of the image at $t + \delta t$ from the image at t, and S_0 is the area of the subsection. In this study, the cross-correlation is calculated for a pair of consecutive images in the time sequence, and hence δt is always about 15 s (see § 2.1). Then we define the pair $(\delta x, \delta z)$ of highest CC as a displacement vector $(\delta \boldsymbol{r})$ at this subsection during δt.

Now the velocity at each subsection can be calculated as $\boldsymbol{v} = \delta \boldsymbol{r}/\delta t$, but there is a problem of accuracy. To increase the statistical accuracy of derived velocities, we take the same average taken by Kitai et al. (1997). First, we take a partial time T out of the total observation time and select a group of images observed during that time. The number of images belonging to this group is represented by n. Then we calculate the correlation between consecutive images in this group and eventually obtain $(n - 1)$ displacement vectors at each subsection. From these $(n - 1)$ vectors, the average velocity at each subsection during T is defined as

$$\langle \boldsymbol{v} \rangle_n \equiv \frac{\sum_{i=1}^{n-1} \delta \boldsymbol{r}_i}{\sum_{i=1}^{n-1} \delta t_i} = \frac{\sum_{i=1}^{n-1} \delta \boldsymbol{r}_i}{T}, \quad (2)$$

where $\{\delta \boldsymbol{r}_i;\ i = 1, 2, \ldots, n - 1\}$ is the displacement vector between the ith and $(i + 1)$th images. In Figure 6, we show the variation of the x-component of average velocity with n at a certain subsection. Clearly, this figure indicates that the amount of fluctuation in average velocity becomes small as n becomes large.

Next, we evaluate the amount of fluctuation in average velocity at all subsections. We calculate $\Delta\langle \boldsymbol{v} \rangle_n / \langle \boldsymbol{v} \rangle_n$ at each subsection, where $\Delta\langle \boldsymbol{v} \rangle_n \equiv \langle \boldsymbol{v} \rangle_{n+1} - \langle \boldsymbol{v} \rangle_n$. Given a certain value of n, 27 × 24 subsections have their own $\Delta\langle \boldsymbol{v} \rangle_n / \langle \boldsymbol{v} \rangle_n$, from which we have made a histogram of how many subsections come into a certain range of $\Delta\langle \boldsymbol{v} \rangle_n / \langle \boldsymbol{v} \rangle_n$. In Figure 7, we show the cases of $n = 35$ ($T = \sum_{i=1}^{34} \delta t_i \sim 500$ s) and 103 ($T \sim 1500$ s) the former represented by dotted lines and the latter by solid lines. From this figure, it is found that the number of subsections having a sufficiently small fluctuation is larger in the case of $n = 103$ than when $n = 35$. In practice, since the average time T must not be over the evolutionary time of photospheric motions, we cannot take too large a value of n. Several previous works show that a few tens of minutes would be appropriate for the average time (see Kitai et al. 1997; Ueno & Kitai 1997), so we calcu-

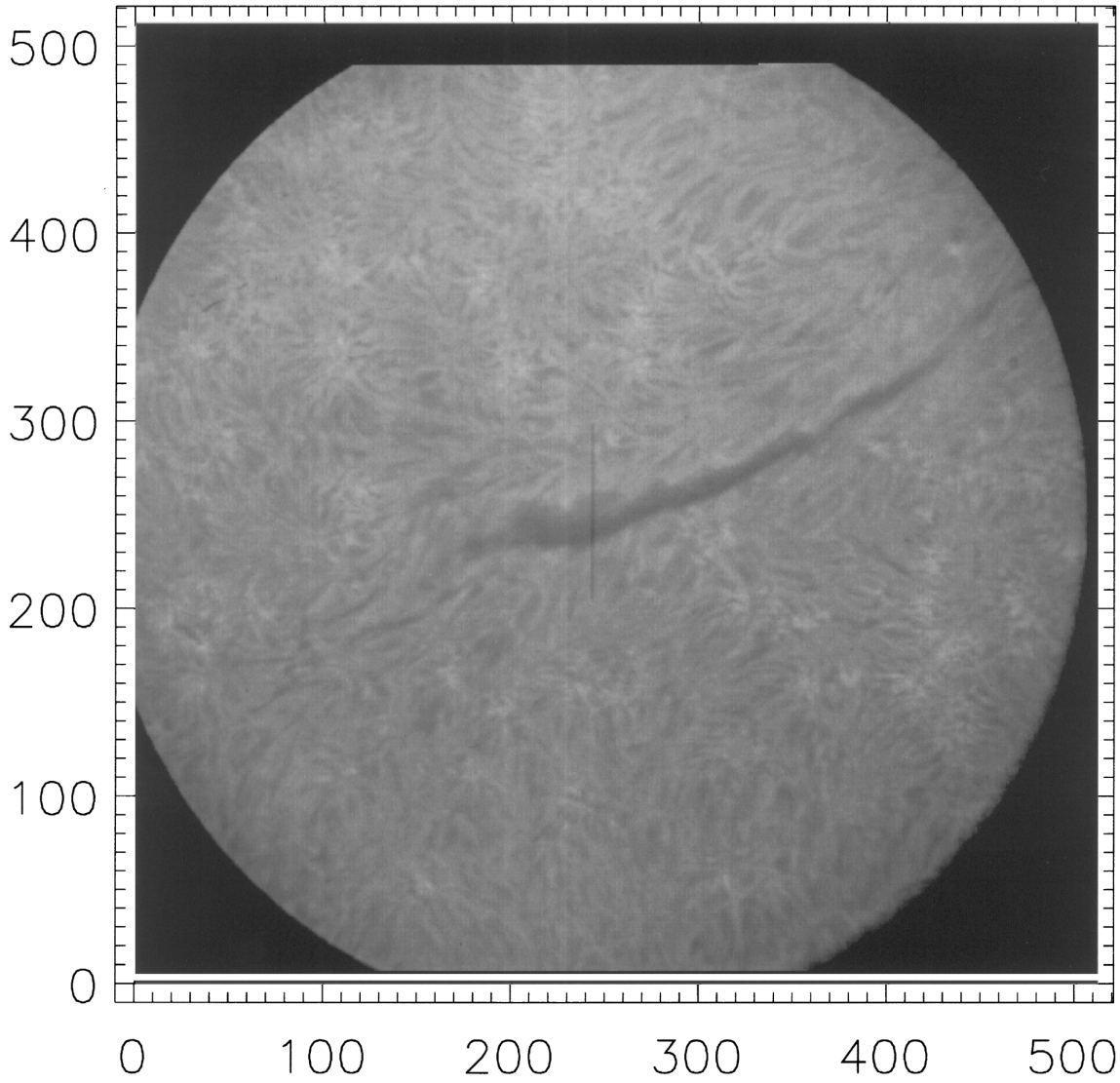

FIG. 3.—Example of filament images in Hα (λ = 6562.8 Å). Pixel dimensions are 512 × 512, and the pixel size is 0.″69, or about 500 km on the solar disk. A dark line can be seen at the center of the image.

late the average velocity during that time at all subsections, which provides a horizontal photospheric velocity field.

The final step of the velocity derivation is to compensate for the effects of systematic image shifting during the observation. This image shifting is caused by solar rotation, other large-scale solar flows, and possible instrumental drifts. To reduce these effects on the velocity field, we subtract the mean velocity over the field of view from the velocity at each subsection. Then we take a 3 × 3 boxcar average on the whole velocity map.

3.2. *Positioning of a Dark Filament on a Granulation Image*

Co-alignment between a filament image and a granulation image has been done by adjusting both dark lines on these two images. Actually, we took images with a dark line on them (see §§ 2.2 and 2.3) by placing a fiducial mark in an intermediate focal plane at the beginning of a sequence of observation and then removed it to take normal images without a dark line. In this way, we can fix the relative position of the filament on the photospheric velocity map derived from granulation images. However, since the formation height of a filament is different from that of granules, and the filament we observed is not at the disk center (see Fig. 1), there is a projection effect in the filament overlaid with the velocity map. Therefore, when we investigate photospheric motions around a filament channel (a photospheric region just below the filament axis), we must take that projection effect into account).

3.3. *Chromospheric Line-of-Sight Velocity Field*

As is mentioned in § 2.3, we observed three types of chromospheric images: Hα center images (λ = 6562.8 Å), blueshifted images (λ = 6562.2 Å), and redshifted images (λ = 6563.4 Å). In general, blueshifted images show areas where upward motions (toward observers) occur, and redshifted images show where downward motions (toward the Sun) occur. Therefore, we can make a line-of-sight velocity map by subtracting a blueshifted image from a redshifted image. This map has information about rising-up (white) and falling-down (black) regions. In practice, both blue-

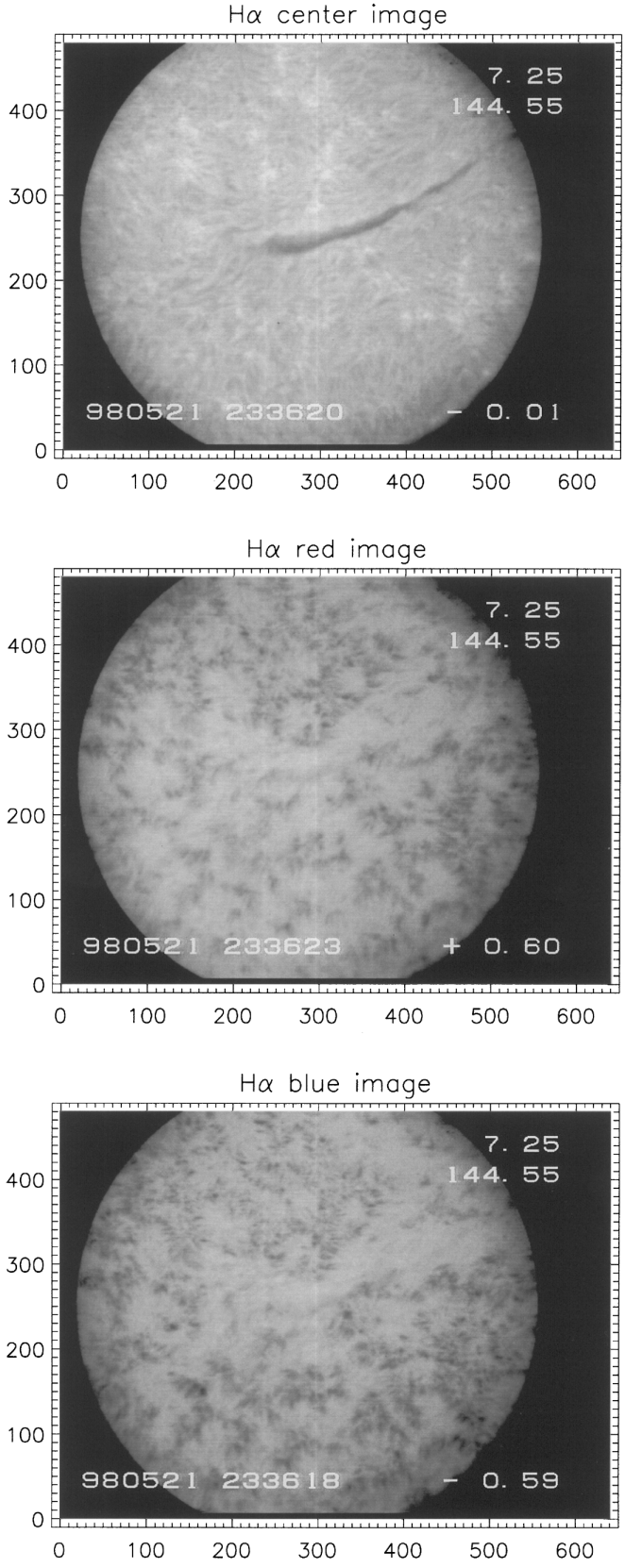

FIG. 4.—Examples of three types of chromospheric images. *Top*: Hα center image ($\lambda = 6562.8$ Å). *Middle*: redshifted image ($\lambda = 6562.8 + 0.6$ Å). *Bottom*: blueshifted image ($\lambda = 6562.8 - 0.6$ Å). Pixel dimensions are 640 × 480, and the pixel size is 0.″69, or about 500 km on the solar disk.

shifted and redshifted images are time-averaged in order to reduce the effects of image shifting and oscillatory motions.

4. RESULTS

4.1. *Photospheric Velocity Field*

Figure 8*a* shows the photospheric velocity field on a filament image, and Figure 8*b* shows the same velocity field associated with a gray-scaled divergence map and two colors of contours of the filament image. The velocity field in these figures is derived from granulation images observed from 23:25 UT to 23:49 UT on 1998 May 21. The divergence map is derived from this velocity field, where white and black areas indicate diverging and converging regions, respectively. As for the filament image, it was taken at 23:01 UT on the same day. White contours in Figure 8*b* represent the apparent position of a filament on a granulation image, and black contours represent the deduced position of a filament channel in the photosphere just below the filament axis. The deviation of the filament channel from the filament axis on the granulation image is estimated by taking into account the formation height of the filament (about 20,000 km), which was measured when the filament was at the solar limb.

From Figures 8*a* and 8*b*, it is found that the velocity of photospheric motions is typically 1 km s^{-1}. When we pay attention to the velocity pattern around the filament channel (*black contour*), we notice that there is a converging region at $x = 360$, $z = 310$. The direction of photospheric flows at the upper side (around $x = 310$, $z = 310$) of this converging region is opposite to the flow direction at its lower side (around $x = 350$, $z = 220$), which means that shearing motions occur in that area. We also find that there is a diverging region at $x = 220$, $z = 250$ in the filament channel. As to the typical size of converging and diverging regions, the diameter is about 50 pixels, corresponding to about 10,000 km, which is almost equal to the size of mesogranules.

Next, we investigate the temporal variation of photospheric motions. Figures 9*a* and 9*b* are similar to Figures 8*a* and 8*b*, except for the observation time, which is almost 6 hours later than Figures 8*a* and 8*b*. From Figure 8*a* and 9*a*, it is found that the filament on the whole maintains a similar shape during 6 hours, although there are some changes due to small but continual motions in the filament. A typical value of photospheric motions is almost the same in both figures (~ 1 km s^{-1}), while their local patterns are different. For example, the region of shearing motions seen in Figure 8*b* disappears in Figure 9*b*. However, looking at the gray-scaled divergence map in both figures, we confirm that most of the diverging and converging regions survive over 6 hours, although their strength has varied. Figure 10 is a correlation diagram of the strength of divergence between Figure 8*b* and 9*b*, which shows a weak positive correlation (correlation coefficient ~ 0.18). Such survival of diverging and converging regions is consistent with the findings of Simon et al. (1988) that there is little evidence of major changes in the averaged flow field over several hours.

4.2. *Chromospheric Line-of-Sight Velocity Field*

As was mentioned in § 3.3, we made time-averaged Hα blueshifted and redshifted images, Figs. 11*a* and 11*b*, respectively. The observation time of these original images is from 23:36 UT to 23:46 UT on 1998 May 21, so this is fairly

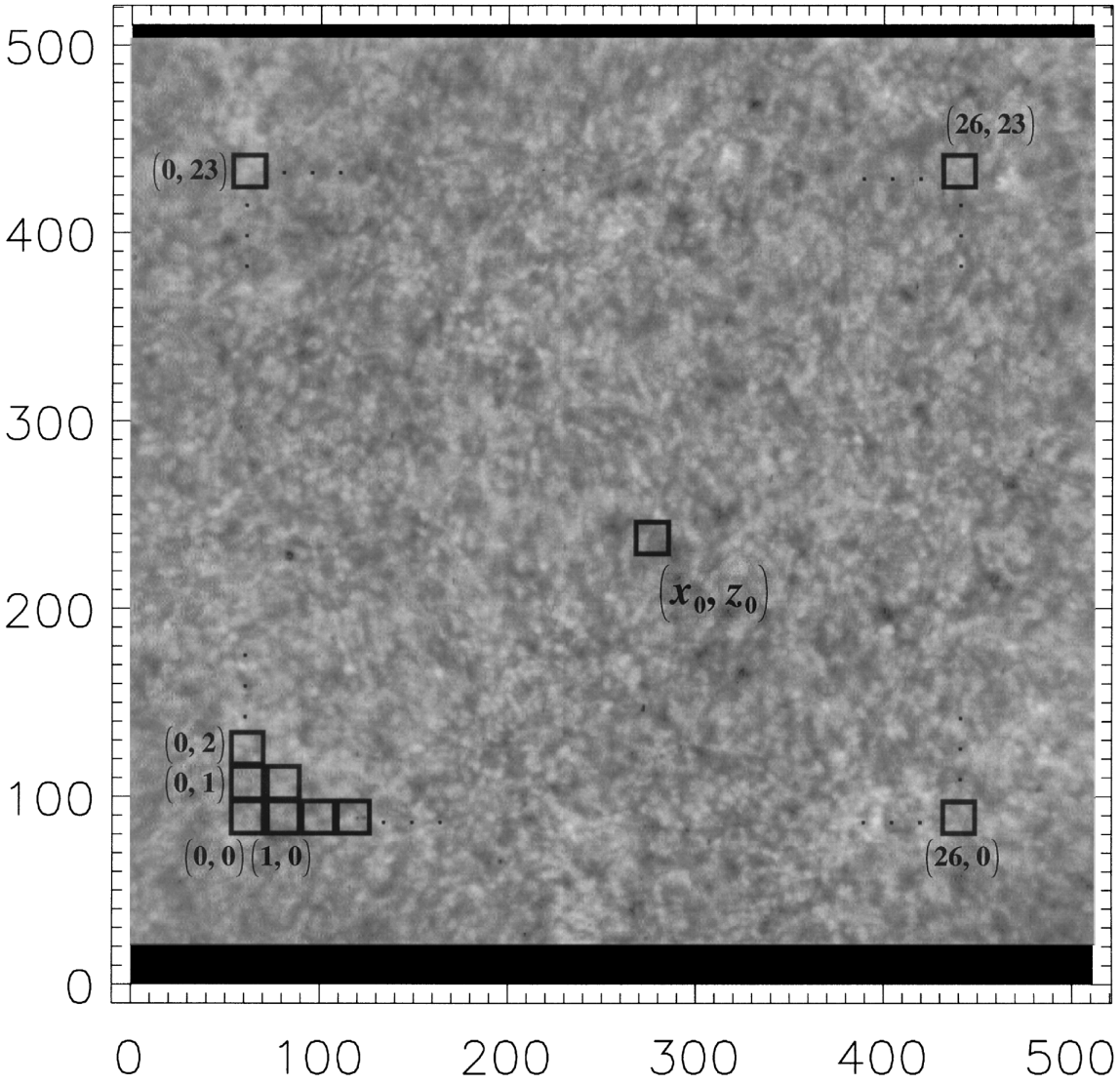

FIG. 5.—Schematic view graph of subsections produced on a granulation image. Each subsection has 15 × 15 pixels, represented by a pair of integers (x_0, z_0), where x_0 is the column number counted from the left side, and z_0 is the row number counted from the bottom. The center of subsection (0, 0) is located 60 pixels from the left side and 85 pixels from the bottom, whereas the center of subsection (26, 23) is 60 pixels from the right side and 80 pixels from the top.

close to the observation time of Figures 8*a* and 8*b*. After doing a shading correction for both images, we subtract the blueshifted image from the redshifted image to make a line-of-sight velocity map, which is displayed in Figure 11*c*. In this velocity map, white areas represent regions where upward motions (toward observers) are dominant and black areas represent regions where downward motions (toward the Sun) are dominant. Figure 11*d* shows an Hα center image whose observation time is 23:36 UT on 1998 May 21. The contours of this center image are overplotted in Figures 11*a*–11*c*.

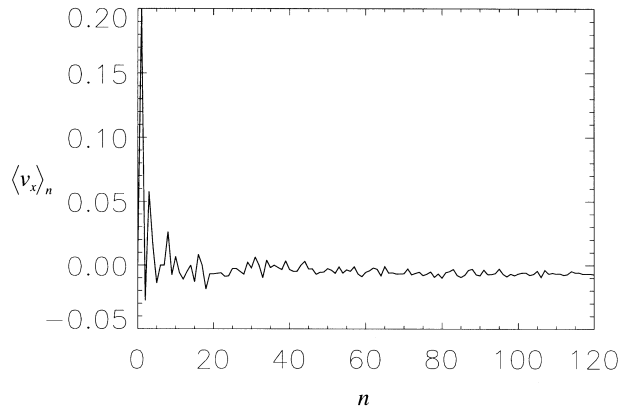

FIG. 6.—Variation of the x-component of average velocity with n at a certain subsection. The velocity is given in pixels s^{-1}.

As for the line-of-sight velocity field inside the filament, Figure 11*c* shows that there is an area of downward motion ($140 \leq x \leq 270, 230 \leq z \leq 250$) at one side of the filament axis and an area of upward motion ($140 \leq x \leq 270$, $210 \leq z \leq 230$) at the other side. This implies that the filament material has a helical motion inside the filament. Another point to be mentioned about this figure is that a ringlike distribution of black spots can be seen in the region of $150 \leq x \leq 280, 320 \leq z \leq 430$. The size of this region is about 30,000 km, which is a typical size of supergranules. We consider that this ring of black spots corresponds to the boundary of a supergranule cell because downward motions are usually stronger there. Moreover, Figure 11*d* shows that magnetically active plages are distributed along

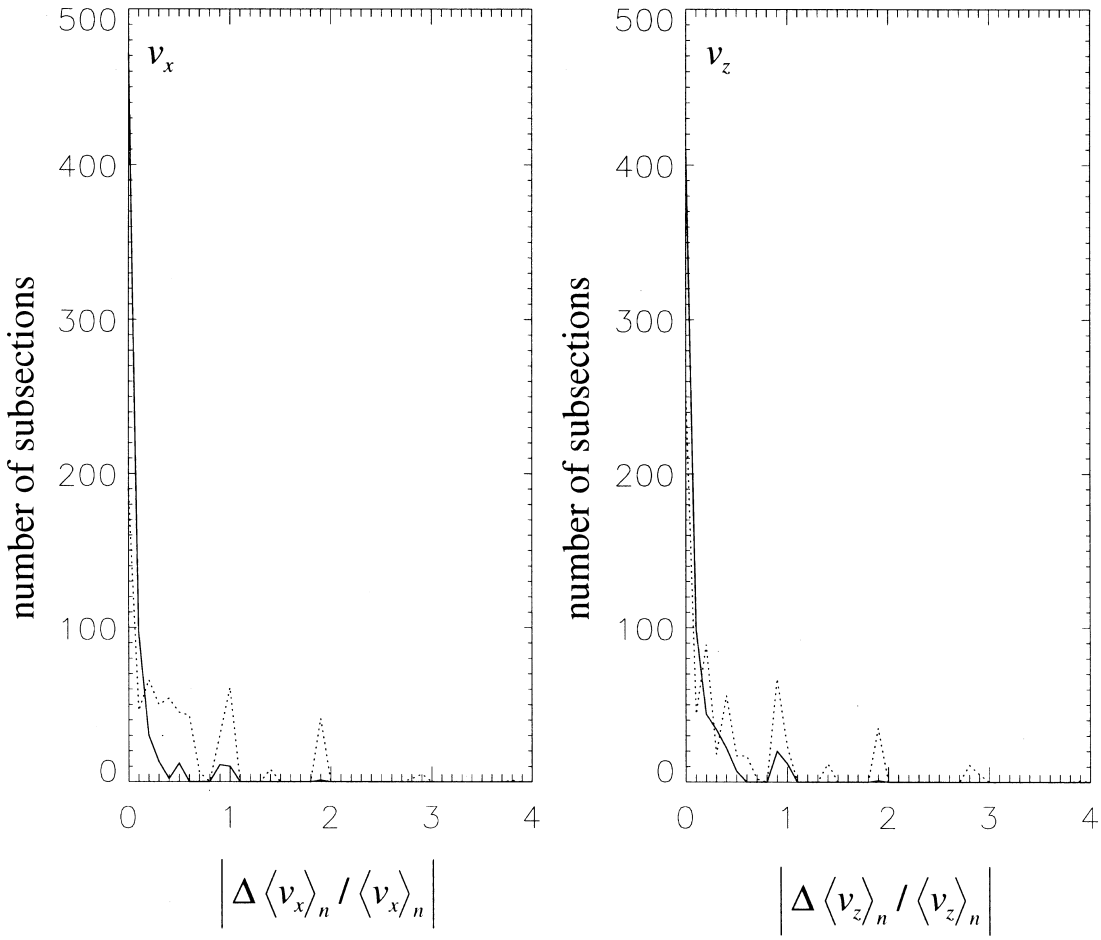

FIG. 7.—Histograms of $|\Delta\langle v_x\rangle_n/\langle v_x\rangle_n|$ and $|\Delta\langle v_z\rangle_n/\langle v_z\rangle_n|$ in the cases of $n = 35$ (*dotted line*) and $n = 103$ (*solid line*). The total number of elements is given by the number of subsections, i.e., $27 \times 24 = 648$ in both cases. The bin size is 0.1.

that ring. This also suggests that this ring lies at the edge of a supergranule, where magnetic fields are usually concentrated.

It may be worth considering, in passing, the comparison of a photospheric velocity field with a chromospheric line-of-sight velocity field. When we pay attention to Figures 11*c* and 8*b*, we find that a diverging region at $x = 240$, $z = 370$ in Figure 8*b* is located at the center of the supergranular cell in Figure 11*c*. This reflects the fact that material moves upward at the center of a supergranule and sinks at the boundary of it.

We then study the temporal variation of a chromospheric line-of-sight velocity field. Figures 12*a*–12*d* are similar to Figures 11*a*–11*d* except for the observation time, which is 05:19 UT–05:28 UT on 1998 May 22. This is close to the observation time of Figures 9*a* and 9*b*.

Comparing Figure 11*c* to Figure 12*c* we notice that a supergranule located at the upper part of the velocity map survives over 6 hours. Since the typical life span of a supergranule is an order of days, it is possible that we observe the same supergranule during several hours. We also find that a diverging region ($x = 220$, $z = 390$) in Figure 9*b* is located at the center of a supergranule in Figure 12*c*. In Figure 11*c* there is an area of downward motion at $x = 350$, $z = 230$, where the so-called "filament foot" forms later (see $x = 340$, $z = 210$ in Figure 12*c*). Schmieder, Raadu, & Wiik (1991) reported that material moving downward at up to 15 km s^{-1} was often seen especially at filament feet.

5. DISCUSSION AND CONCLUSION

The results we presented above provide important information on theories of filament formation. In the following, we discuss what our results suggest regarding previously proposed filament models and what kinds of observational results are still needed for understanding the exact formation processes of filaments.

From a theoretical viewpoint, motions converging toward a filament channel relate to a filament's formation and activity (van Ballegooijen & Martens 1989; Anzer 1990; Inhester et al. 1992; Choe & Lee 1992; Ridgway & Priest 1993; Priest et al. 1994; Priest et al. 1996; Kuijpers 1997). However, our results do not show that only a converging region exists along a filament channel. Figures 8*b* and 9*b* show that there is not only a converging region but also a diverging region in a filament channel in the photosphere. It is therefore not possible to conclude from the present study, that the filament was formed only by converging flows; that is, there may be other factors in filament formation, or there could have been a converging region all along the filament channel before our observation began. To make this clear, we have to study the whole life of a filament, especially the beginning phase of filament formation. Another topic to be mentioned is filament activities. By comparing Figure 8*b* and Figure 9*b*, we find that a converging region continues to exist around $x = 370$, $z = 300$ in both figures. Since the filament is formed

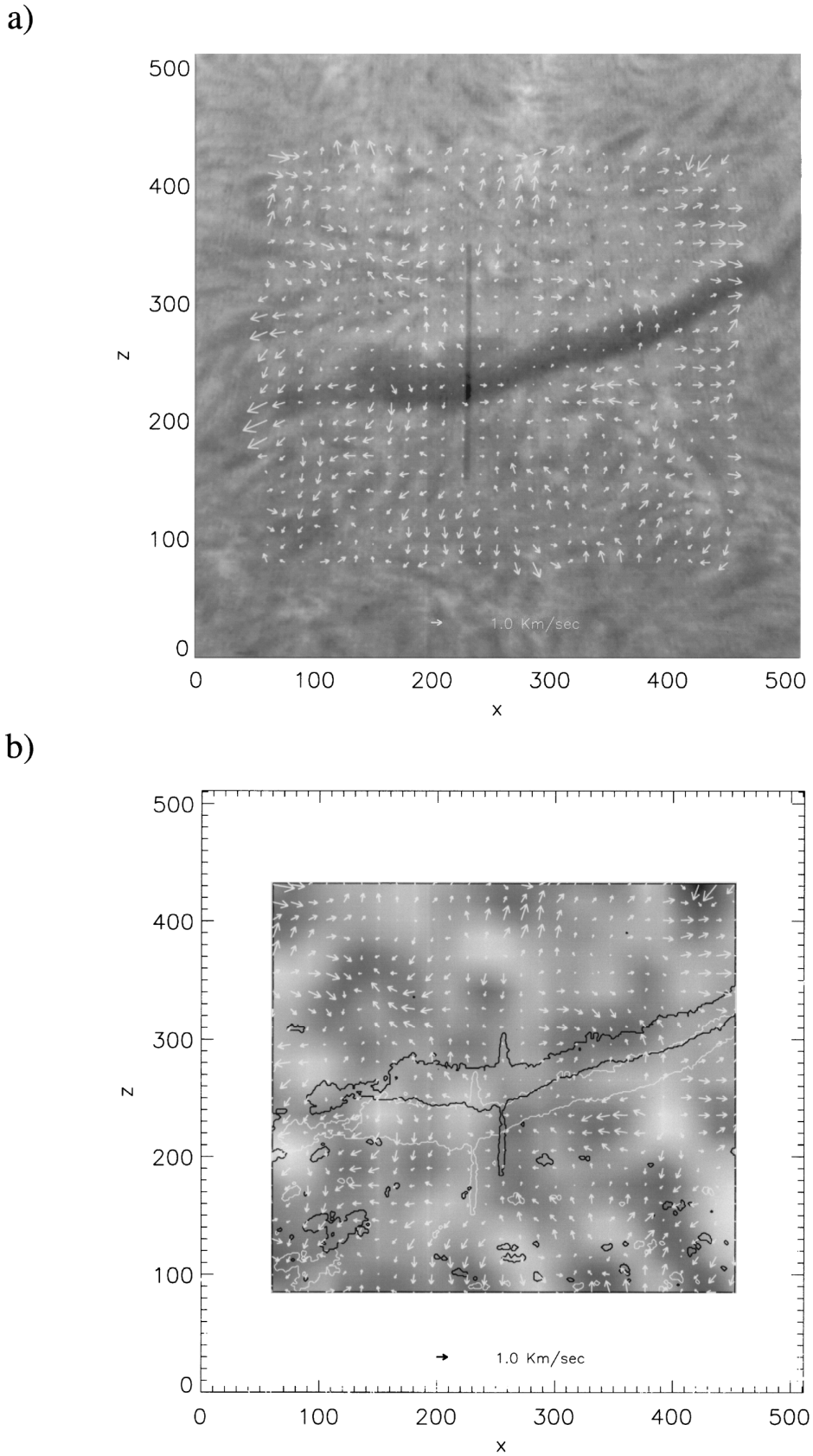

FIG. 8.—(*a*) Photospheric velocity map derived from granulation images (observation time: 1998 May 21, 23:25 UT–1998 May 21, 23:49 UT), overlaid on an image of filament observed at 23:01 UT on the same day. (*b*) Same velocity map, associated with a gray-scaled divergence map and two colors of contours of the filament image. White and black areas on this map indicate diverging and converging regions, respectively. White contours represent the apparent position of the filament, and black contours represent the deduced position of the filament channel in the photosphere just below the filament axis. Both figures show a fiducial dark line on the image. In these figures, 1 pixel corresponds to about 240 km.

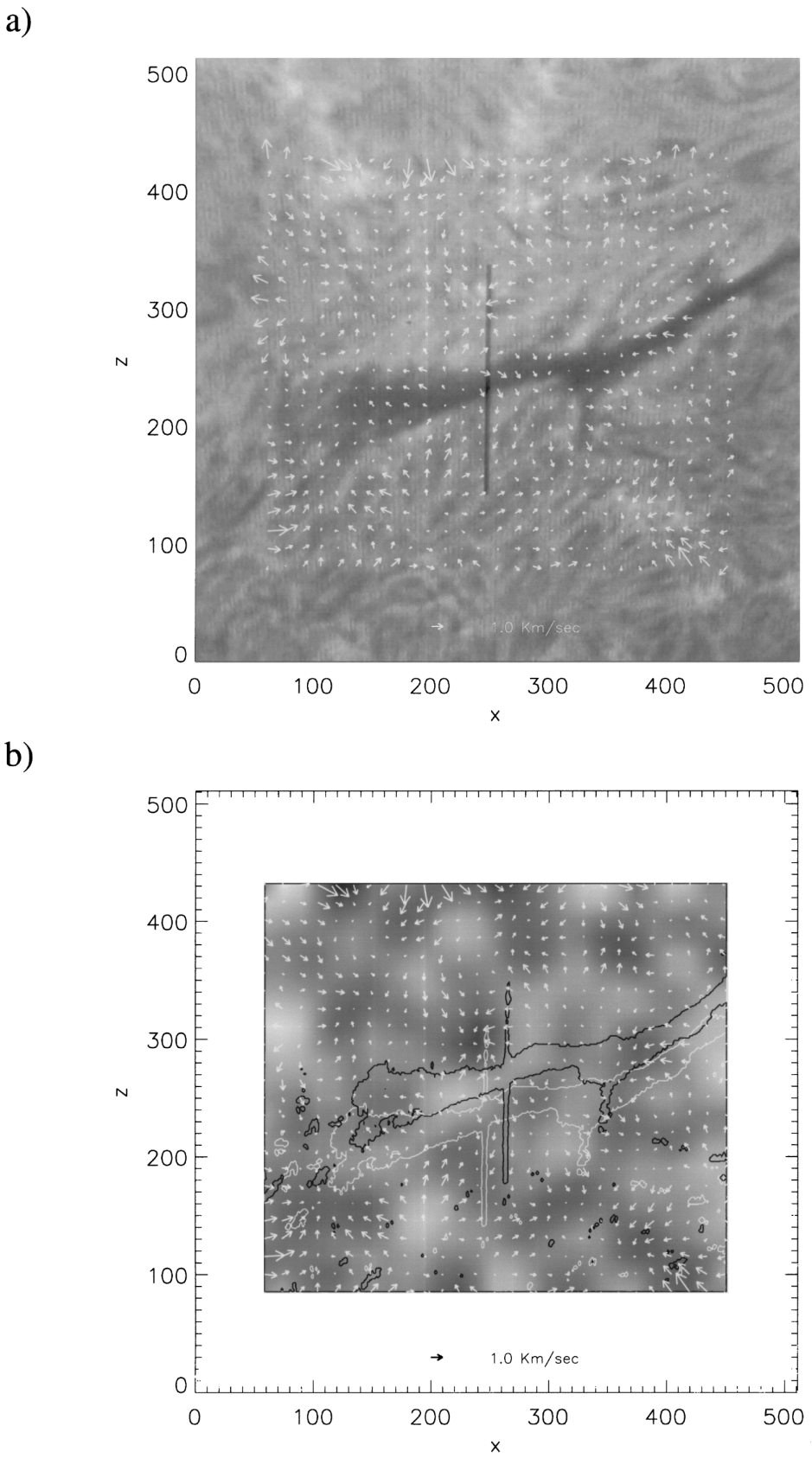

FIG. 9.—Same as Figs 8*a* and 8*b*, except for the observation time, which is 05:19 UT–05:46 UT on 1998 May 22 for granulation images and 05:06 UT on the same day for the filament image.

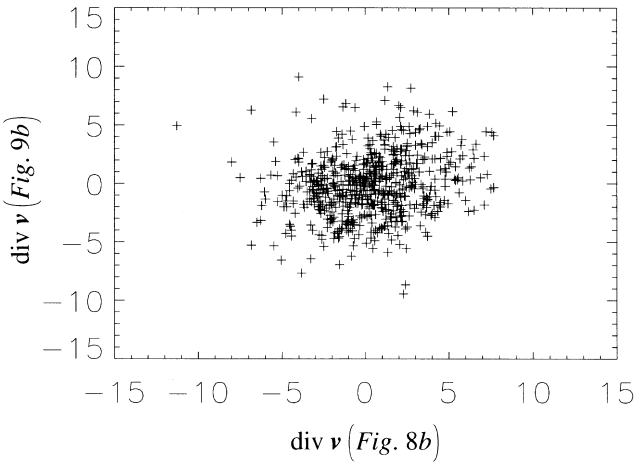

FIG. 10.—Correlation diagram of the strength of divergence between Figs 8*b* and 9*b*.

between those regions of opposite magnetic polarities (see Figure 13), a long-lived converging region could make it possible for opposite magnetic polarities to approach each other and then magnetically reconnect. As to activities seen in filaments, we know of the "pivot points" that Mouradian et al. (1987), Martres, Mouradian, & Soru-Escaut (1986) and Zuccarello (1992) reported. This is a singular point in the filament that rotates at the Carrington velocity at least 3 times, while other parts of the filament have their own motion deviated from solar rotation. The important property of pivot points is that flare activity often occurs around them. It is an attractive idea that an underlying photospheric converging region in a filament channel is related to a pivot point in the filament, although we cannot confirm this because the present study does not have sufficient time to follow the long-term evolution of the converging region and its counterpart in the filament.

Next, let us turn to "filament eruption," which is a very interesting topic for solar physicists. Since a filament is part of a large-scale magnetic structure, its eruption has a close connection to the dynamics of magnetic structure. Here filament eruption is connected with the rising motion of a magnetic arcade. Observationally, Schmieder et al. (1984) found that filaments showed a slight net blueshift in the transition region. The theoretical study of the evolution of a magnetic arcade has been done by many authors (for a review see Low 1996). Shearing motions imposed on the footpoints of a magnetic arcade are one of several mechanisms causing the eruption of the arcade. The essence of this mechanism is to generate a strong longitudinal magnetic field along a filament channel, which supplies the main part of the magnetic energy for that eruption. Our results show that there is an area where shearing motions occur in Figure 8*b* (around $x = 310$, $z = 310$ and around $x = 350$, $z = 220$). However, these are not steady motions, because the area disappears in Figure 9*b*, which displays the velocity map 6 hours later than Figure 8*b*. We therefore conclude that there are no long-lived (longer than several hours) shearing motions around the filament channel in the present study. As Priest et al. (1996) say, a strong longitudinal magnetic field along a filament channel can be formed through other physical processes without shearing motions. They show one of these processes, in which continual emergence of flux tubes and the subsequent reconnection between them can produce a strong longitudinal magnetic field along the filament channel. Nevertheless, the effect of shearing motions on filament eruption is still unclear, because the filament presented in this paper was in a quiet state throughout the observation and did not show any large-scale eruption. In order to understand the effect exactly, we must study in detail the temporal evolution of a photospheric velocity field around active filaments.

Helical motions inside the filament provide important evidence that filament material is covered by helical magnetic fields. Vrsnak, Ruzdjak, & Rompolt (1991) report that filaments had a helical structure and made a twisting motion when they erupted. Theoretically, two models have been proposed to explain the generation of a helical magnetic field in the corona. One starts with a simple magnetic arcade, subject to shearing motions on its footpoints. Then magnetic reconnection occurs within the arcade, forming a helical magnetic field over the photosphere. Hence this model is again based on the role played by shearing motions in the filament physics. Another starts with a helical flux tube, rising from the subphotosphere by magnetic buoyancy. A major difference between this model and the former one is that a helical structure of magnetic fields has already formed before they emerge on the photosphere. The latter model therefore implies the emergence of a twisted magnetic flux tube, which has been reported in some papers (e.g., Kurokawa 1989). Recently, in connection with studies of coronal mass ejections (CMEs), "twisted flux tube" model has been developed by many authors (Low 1994; 1997; Low & Hundhausen 1995; Chen 1997; Wu & Guo 1997; Rust 1997; Rust & Kumar 1995; Bothmer & Rust 1997; Bothmer & Schwenn 1994). According to this model, convective motions could play an important role in generating a twisted flux tube under the photosphere.

There are also several findings about the twisted flux tube model. Martin, Bilimoria, & Tracadas (1994) find a new nature of filament whereby filaments are divided into two categories: dextral sinistral. Rust & Kumar (1995) explain this classification by considering the sign of helicity and the orientation of a twisted flux tube. Very recently, Aulanier & Démoulin (1998) showed an interesting finding that magnetic fields having a dip structure to support filament-foot material appeared around a twisted flux tube.

The photospheric velocity map we present in this paper provides new important information on theories of filament formation. Combined with three-dimensional MHD simulations (Magara 1998), it can be used to check the validity of theoretical models by comparing the theoretical velocity field with the velocity map in Figures 8*b* and 9*b*. In this way, we can make a more reliable model by which we reproduce visible aspects of filament as well as clarify invisible physical processes operating in its background.

We would like to thank M. Kadota for her assistance in preparing some figures in this paper. We also gratefully acknowledge helpful discussions with K. Yoshimura, T. Ishii, and H. Kouzu as well as the instructive suggestions of the anonymous referee. Finally, our special thanks are due to NSO/Kitt Peak for permission to use the data, which are produced cooperatively by NSF/NOAO, NASA/GSFC, and NOAA/SEL.

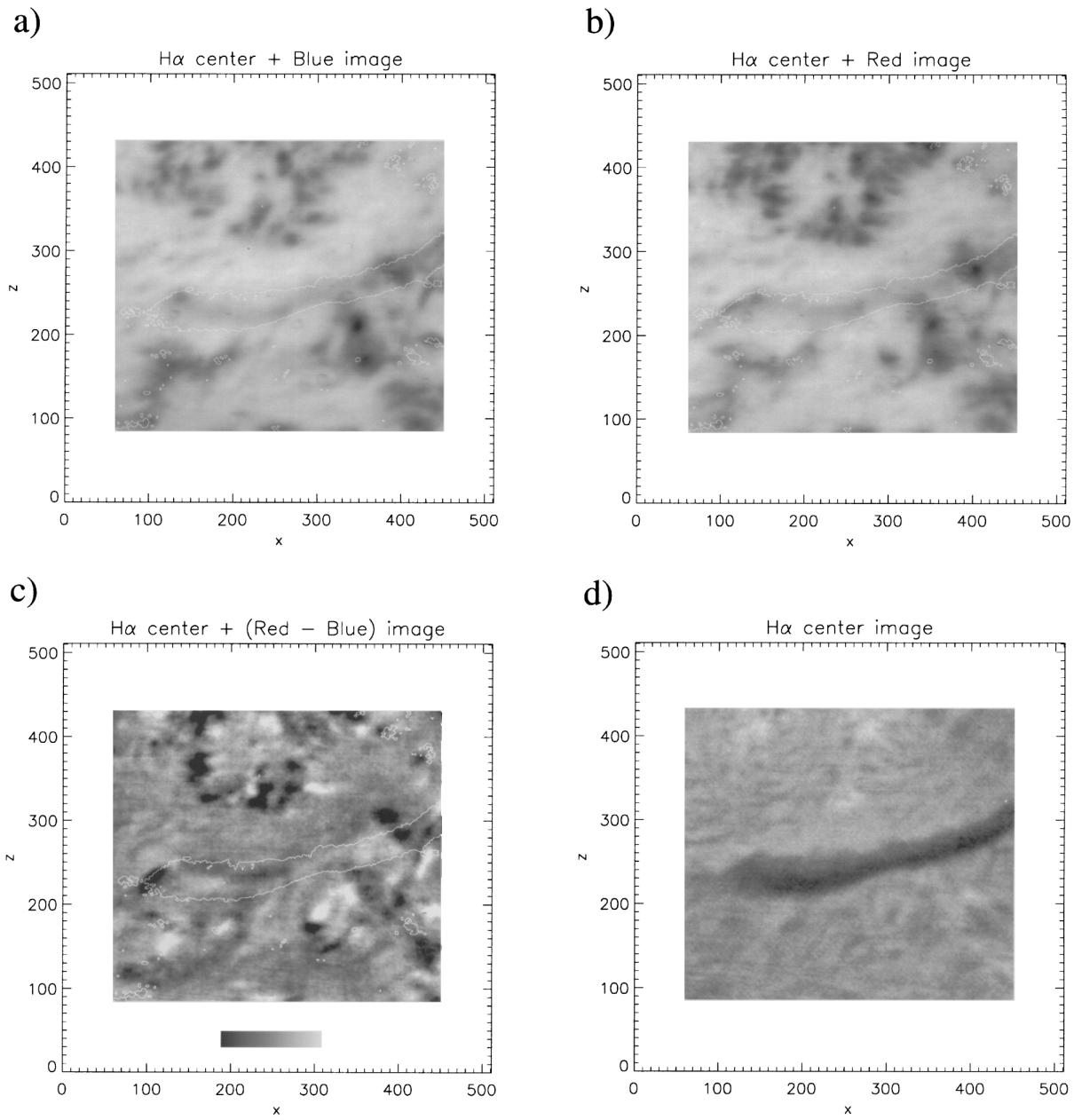

FIG. 11.—(*a*) Time-averaged blueshifted Hα image, associated with contours of an Hα center image. (*b*) Time-averaged redshifted Hα image, associated with contours of an Hα center image. (*c*) Line-of-sight velocity map derived from blueshifted and redshifted images, associated with contours of an Hα center image. White areas represent regions where upward motions (towards observers) are dominant, and black areas represent where downward motions (toward the Sun) are dominant. (*d*) Hα center image displayed in gray scale. The observation time is 23:36 UT–23:46 UT on 1998 May 21. In these figures, 1 pixel corresponds to about 240 km.

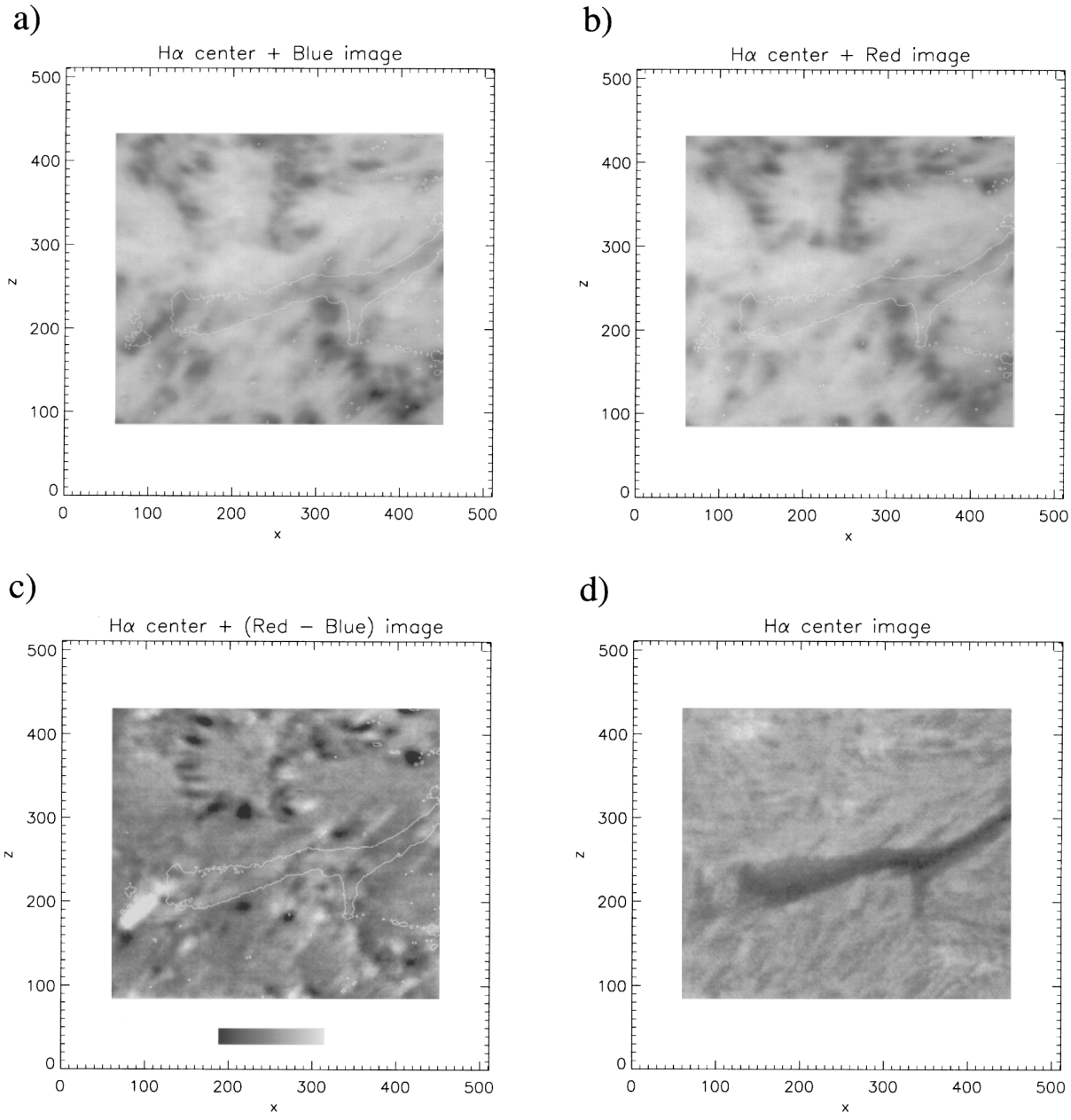

FIG. 12.—Same as Figs 11*a*–11*d*, except for the observation time, which is 05:19 UT–05:28 UT on 1998 May 22

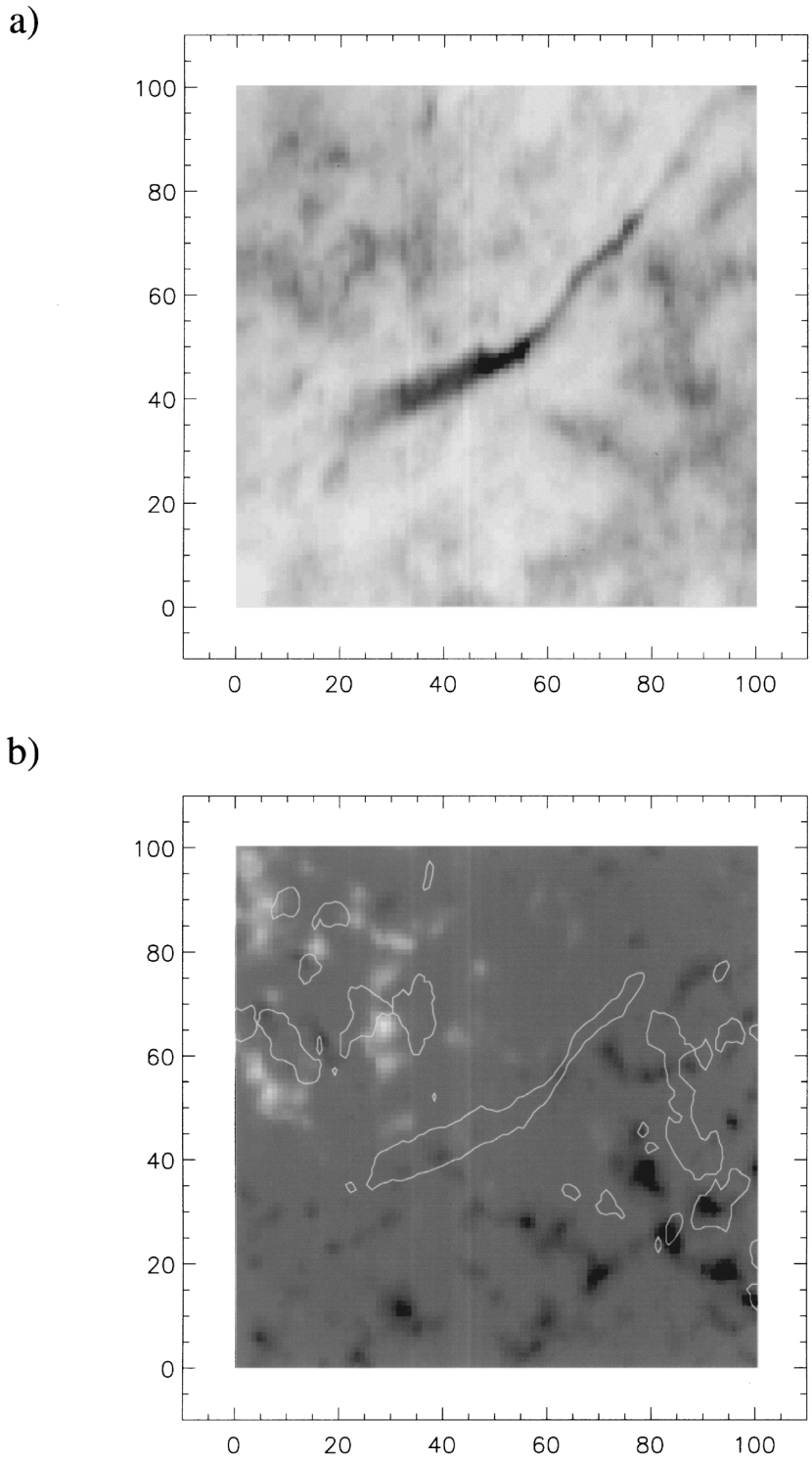

FIG. 13.—(*a*) He 10830 Å image observed 15:50 UT–16:30 UT on 1998 May 22 using the NSO Vacuum Telescope located at Kitt Peak. (*b*) Magnetogram observed 14:45 UT–15:40 UT on the same day in Kitt Peak, associated with contours of the He 10830 Å image. In these figures, 1 pixel corresponds to 2″, or about 1400 km.

REFERENCES

Anzer, U. 1990 Sol. Phys., 130, 403
Aulanier, G., & Démoulin, P. 1998 A&A, 329, 1125
Bothmer, V., & Rust, D.M. 1997 in Coronal Mass Ejections, ed. N. Crooker, J. A. Joselyn, & J. Feynman (Washington, DC: AGU) 139
Bothmer, V., & Schwenn, R. 1994, Space Sci. Rev., 70, 215
Brandt, P. N., Scharmer, G. B., Ferguson, S. H., Shine, R. A., Tarbell, T. D., & Title, A. M. 1988, Nature, 335, 238
Chen, J. 1997 in Coronal Mass Ejections, ed. N. Crooker, J. A. Joselyn, & J. Feynman (Washington, DC: AGU) 65
Choe, G. S., & Lee, L. C. 1992, Sol. Phys., 138, 291
Inhester, B., Birn, J., & Hesse, M. 1992, Sol. Phys., 138 257
Kitai, R., Funakoshi, Y., Ueno, S., Sano, S., & Ichimoto, K. 1997, PASJ, 49, 513
Kuijpers, J. 1997, ApJ, 489, L201
Kurokawa, H. 1989, Space Sci. Rev., 51, 49
Low, B. C. 1994, Plasma Phys., 1, 1684
——— 1996, Sol. Phys., 167, 217
——— 1997, in Coronal Mass Ejections, ed. N. Crooker, J. A. Joselyn, & J. Feynman (Washington, DC: AGU) 39
Low, B. C., & Hundhausen, J. R. 1995, ApJ, 443, 818
Magara, T. 1998, Ph.D. thesis, Univ. Kyoto
Martin, S. F., Bilimoria, R., & Tracadas, P. W. 1994, in Solar Surface Magnetism, ed. R. J. Rutten & C. J. Schrijver (New York: Springer), 303
Martin, S. F., Livi, S. H. B., & Wang, J. 1985, Australian J. Phys., 38, 929
Martres, M. J., Mouradian, Z., & Soru-Escaut, I. 1986, A&A, 161, 376
Mouradian, Z., Martres, M. J., Soru-Escaut, I., & Gesztelyi, L. 1987, A&A, 183, 129
November, L. J. 1986, Appl. Opt., 25, 392
November, L. J., & Simon, G. W. 1988, ApJ, 333, 427
Priest, E. R., & Forbes, T. G. 1990, Sol. Phys., 130, 399
Priest, E. R., Parnell, C. E., & Martin, S. F. 1994, ApJ, 427, 459
Priest, E. R., van Ballegooijen, A. A., & MacKay, D. H. 1996, ApJ, 460, 530
Ridgway, C., & Priest, E. R. 1993, Sol. Phys., 146, 277
Rust, D. M. 1997, in Coronal Mass Ejections, ed. N. Crooker, J. A. Joselyn, & J. Feynman (Washington, DC: AGU) 119
Rust, D. M., & Kumar, A. 1995, Sol. Phys., 155, 69
Schmieder, B., Malherbe, J. M., Mein, P., & Tandberg-Hanssen, E. 1984, A&A, 136, 81
Schmieder, B., Raadu, M. A., & Wiik, J. E. 1991, A&A, 252, 353
Simon, G. W., et al. 1988, ApJ, 327, 964
Title, A. M., et al. 1989, in Proc. Third Int. Workshop of the OAC and the NATO Advanced Research Workshop on Solar and Stellar Granulation, ed. R. J. Rutten & G. Severino (Dordrecht: Kluwer) 225
Ueno, S., & Kitai, R. 1997, PASJ, 50, 125
van Ballegooijen, A. A., & Martens, P. C. H. 1989, ApJ, 343, 971
Vrsnak, B., Ruzdjak, V., & Rompolt, B. 1991, Sol. Phys., 136, 151
Wu, S. T., & Guo, W. P. 1997, in Coronal Mass Ejections, ed. N. Crooker, J. A. Joselyn, & J. Feynman (Washington, DC: AGU) 83
Yi, Z., & Molowny-Horas, R. 1992, in Proc. LEST Mini-Workshop, Software for Solar Image Processing, ed. Z. Yi, T. A. Darvann, & R. Molowny-Horas, (LEST Tech. Rep. 56) 69
Zuccarello, R. 1992, A&A, 257, 298